Article

Dirac mass induced by optical gain and loss

https://doi.org/10.1038/s41586-024-07664-x

Received: 25 September 2023

Accepted: 4 June 2024

Letian Yu[1,4], Haoran Xue[2,4], Ruixiang Guo[1,3], Eng Aik Chan[1,3], Yun Yong Terh[1], Cesare Soci[1,3] ✉, Baile Zhang[1,3] ✉ & Y. D. Chong[1,3] ✉

Mass is commonly considered an intrinsic property of matter, but modern physics reveals particle masses to have complex origins[1], such as the Higgs mechanism in high-energy physics[2,3]. In crystal lattices such as graphene, relativistic Dirac particles can exist as low-energy quasiparticles[4] with masses imparted by lattice symmetry-breaking perturbations[5–8]. These mass-generating mechanisms all assume Hermiticity, or the conservation of energy in detail. Using a photonic synthetic lattice, we show experimentally that Dirac masses can be generated by means of non-Hermitian perturbations based on optical gain and loss. We then explore how the spacetime engineering of the gain and loss-induced Dirac mass affects the quasiparticles. As we show, the quasiparticles undergo Klein tunnelling at spatial boundaries, but a local breaking of a non-Hermitian symmetry can produce a new flux non-conservation effect at the domain walls. At a temporal boundary that abruptly flips the sign of the Dirac mass, we observe a variant of the time-reflection phenomenon: in the non-relativistic limit, the Dirac quasiparticle reverses its velocity, whereas in the relativistic limit, the original velocity is retained.

The process by which relativistic particles acquire mass is a topic of great relevance to numerous areas of physics. In elementary particle physics, researchers are still investigating the details of how the Higgs field, discovered experimentally in 2012, imparts mass to fermions and bosons[2,3,9], and the mathematical derivation of the Yang–Mills mass gap is one of the unsolved Millennium Problems[10]. Meanwhile, in low-energy physics, the key features of relativistic particles, including mass, can manifest through the quasiparticles of materials such as graphene[4]. Adding a mass to these 'relativistic' quasiparticles is equivalent to lifting a point degeneracy in the band structure[5–8] and can be achieved through several different lattice perturbations, which are also associated with different topological phases of matter[5,11].

Are there any previously unexplored mechanisms for adding mass to a relativistic particle or quasiparticle? It is notable that previous mechanisms have all assumed Hermiticity, the symmetry responsible for the conservation of energy in detail. However, in the fast-developing field of non-Hermitian and non-equilibrium systems[12,13], we can deliberately design structures that break Hermiticity, such as by incorporating gain and/or loss (that is, energy transfer with an unmonitored external system). Certain non-Hermitian lattices, such as those having 'unbroken parity/time-reversal symmetry', are known to host stable quasiparticles that do not blow up or decay over time[14,15]. Unfortunately, Dirac quasiparticles, the simplest type of relativistic quasiparticle, are usually spoiled by gain and loss. Previous studies have found that the introduction of gain and loss turns Dirac point degeneracies into pairs of exceptional points (EPs) or rings of EPs[16–18], which behave very differently from Hermitian degeneracies such as Dirac points[12,19,20]. Band energies do not remain real everywhere in the vicinity of an EP, destabilizing quasiparticle wavefunctions[16,19]. EPs also fuse bands together, necessitating alternative formulations of non-Hermitian band topology in which Dirac quasiparticles play no special role[12].

Here we experimentally demonstrate that gain and loss can be used to create stable massive relativistic quasiparticles. We implement a looped optical-fibre apparatus hosting a synthetic lattice[21] whose band structure has a Dirac point in the Hermitian limit. Applying gain and loss, according to a specific 'semi-Hermitian' symmetry[22,23], opens a relativistic mass gap (see Supplementary Information). Although the overall Hamiltonian is non-Hermitian, the two participating bands obey an effective Dirac Hamiltonian with a real relativistic mass, whose sign and magnitude can be controlled through the gain and loss level. Although it was previously known that certain non-Hermitian bands can exhibit real band energies (for example, through unbroken parity/time-reversal symmetry[14,15]), the use of gain and loss to generate a real mass for a Dirac quasiparticle has, to our knowledge, never been demonstrated.

By controlling the gain and loss in the synthetic lattice, we find several interesting quasiparticle behaviours at spatial and temporal boundaries.

First, we investigate Klein tunnelling, a counterintuitive property of the Dirac equation that allows particles to pass through a potential barrier with height V exceeding the rest energy of the particle Mc^2 (in which M is the rest mass and c is the speed of light)[24,25]. Although the Klein tunnelling of massless Dirac particles has recently been demonstrated in a phononic crystal[26,27], the phenomenon has yet to be studied experimentally for massive Dirac particles. We find that the Dirac quasiparticles in our lattice indeed exhibit Klein tunnelling consistent with the Hermitian theory (for example, total flux is conserved), contingent on semi-Hermiticity being preserved at the boundary. On the other hand, certain boundary choices can violate this symmetry, resulting in an anomalous variant of Klein tunnelling for which flux conservation fails at the boundary despite the quasiparticles having real Dirac masses on each side[23].

---

[1]Division of Physics and Applied Physics, School of Physical and Mathematical Sciences, Nanyang Technological University, Singapore, Singapore. [2]Department of Physics, The Chinese University of Hong Kong, Sha Tin, Hong Kong, China. [3]Centre for Disruptive Photonic Technologies, Nanyang Technological University, Singapore, Singapore. [4]These authors contributed equally: Letian Yu, Haoran Xue. ✉e-mail: csoci@ntu.edu.sg; blzhang@ntu.edu.sg; yidong@ntu.edu.sg

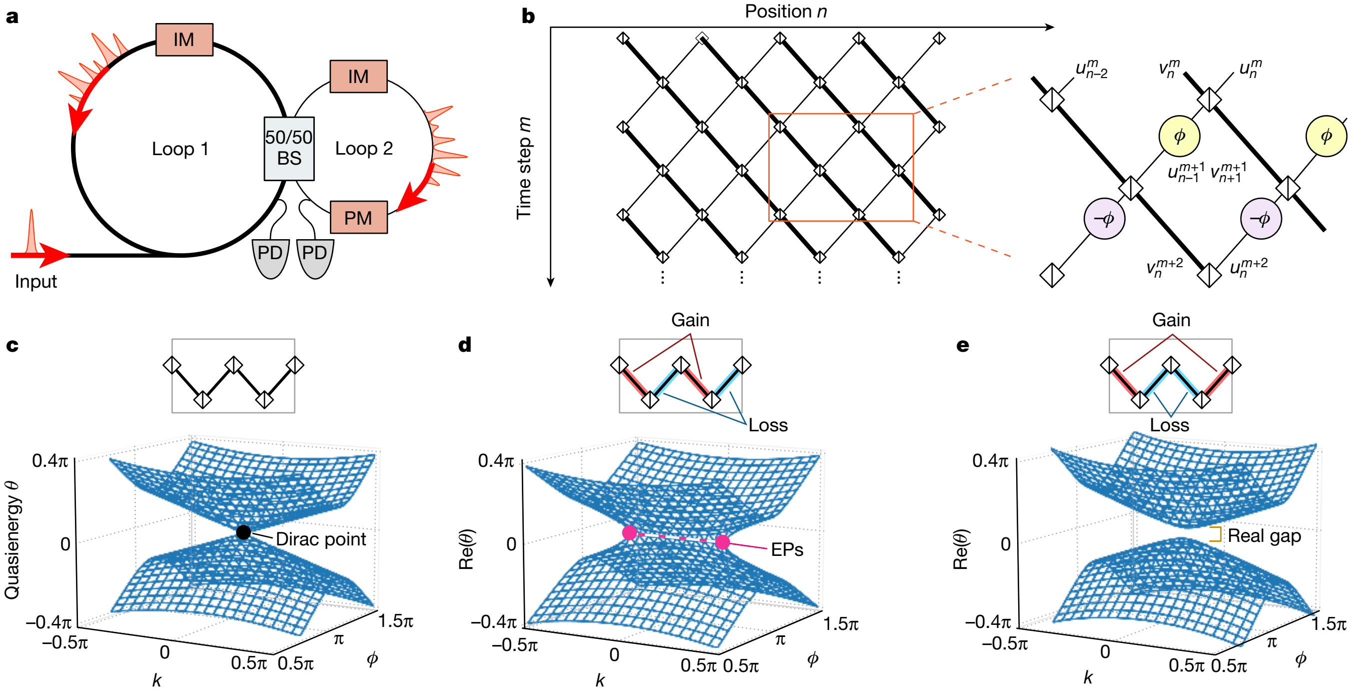

Fig. 1 | Scheme for realizing a non-Hermitian synthetic lattice. a, Schematic of the experiment. Two optical-fibre loops are coupled by a 50/50 beam splitter (BS). Each fibre loop has an intensity modulator (IM), which can alter the amplitude of individual pulses. The short loop has a phase modulator (PM) to vary the phase of incoming signals. The pulses are measured by photodetectors (PDs) placed just before the BS. **b**, The synthetic lattice that the pulse-train evolution maps onto. The index n in each pulse train maps to a spatial position and the number of round trips m maps to time. Inset, definitions of wavefunction amplitudes in the synthetic lattice. **c**–**e**, Schematics of the distribution of gain and loss in the synthetic lattice (top) and the resulting quasienergy spectrum (bottom). The Hermitian case (**c**) exhibits a Dirac point at $k = 0$, $\phi = \pi$. Gain and loss can turn this into a pair of EPs (**d**) or a real mass gap (**e**). In **d** and **e**, the gain and loss level is $g = 0.41$. Only the two bands closest to quasienergy $\theta = 0$ are plotted.

Second, we investigate the consequences of modulating the Dirac mass in time and, specifically, abruptly reversing of its sign. We find that such a 'temporal boundary' leads to an interesting form of time reflection[28–32], or time reversal of the quasiparticle wavefunction. Recently, time reflection has been demonstrated in several notable experiments on water waves, electric waves, cold atoms and other systems not described by the Dirac equation. In the present synthetic lattice, we show that a mass-flipping temporal boundary selectively induces time reflection when the massive Dirac quasiparticle is in the non-relativistic regime, through a state transfer between the upper and lower bands, an effect similar to that of time reversal on a particle (see Supplementary Information). In the relativistic regime, however, the quasiparticle is unaffected by the temporal boundary.

Implementation of photonic synthetic lattice

Our experiment is based on a pair of coupled looped optical fibres (Fig. 1a and Extended Data Fig. 1). A single optical pulse is initially injected into loop 1, which is connected to the shorter loop 2 by a 50/50 beam splitter. The initial pulse evolves into two pulse trains (one in each loop), which undergo repeated splitting and recombination at the beam splitter. The evolution of the pulse train maps onto a discrete-time 'light walk' of a particle in a 1D synthetic lattice (Fig. 1b), as established in previous works[21,33]. The discrete position along each pulse train maps to the discrete lattice position n; the number of round trips the pulses have undergone map to the discrete time step m; and for each (n, m), the pulses in loops 1 and 2 represent right-moving and left-moving wave amplitudes in the synthetic lattice, denoted by v_n^m and u_n^m, respectively (Fig. 1b, inset). For further details of the experimental setup, see Methods.

Several electro-optical modulators, attached to the fibre loops, act as phase modulators and intensity modulators (Fig. 1a). The phase modulator in loop 2 applies a time-dependent phase modulation

$$\Phi(m) = (-1)^m \phi, \tag{1}$$

in which ϕ is a tunable phase parameter. The intensity modulators, acting alongside fibre amplifiers[21], apply a spatially varying gain and loss factor $F(n)$ to each loop. The resulting evolution equations are

$$\begin{aligned} u_n^{m+1} &= \frac{1}{\sqrt{2}}(u_{n+1}^m + \mathrm{i}v_{n+1}^m)F(n)\mathrm{e}^{\mathrm{i}\Phi(m)}, \\ v_n^{m+1} &= \frac{1}{\sqrt{2}}(\mathrm{i}u_{n-1}^m + v_{n-1}^m)F(n-1). \end{aligned} \tag{2}$$

For each n, we let $F(n)$ take two possible values,

$$F(n) = \begin{cases} \mathrm{e}^{g/2}, & \text{(gain)} \\ \mathrm{e}^{-g/2}, & \text{(loss)} \end{cases}, \tag{3}$$

in which g parameterizes the gain and loss level.

Consider the Hermitian case, $g = 0$. This lattice is translationally symmetric in both space and time, with period $\Delta n = \Delta m = 2$ (Fig. 1b, inset). We take a Floquet–Bloch ansatz[34]

$$\begin{pmatrix} u_n^m \\ v_n^m \end{pmatrix} = \begin{pmatrix} U \\ V \end{pmatrix} \exp\left[-\frac{\mathrm{i}m\theta}{\Delta m} + \frac{\mathrm{i}kn}{\Delta n}\right], \tag{4}$$

in which k is the quasimomentum and θ is the quasienergy (both real). Substituting into equation (2), we obtain the Floquet band structure shown in Fig. 1c, in which θ is plotted against k and the phase parameter ϕ (which serves as an extra parametric dimension[33]). It exhibits a Dirac point at $k = \theta = 0$, $\phi = \pi$. (There is another Dirac point at

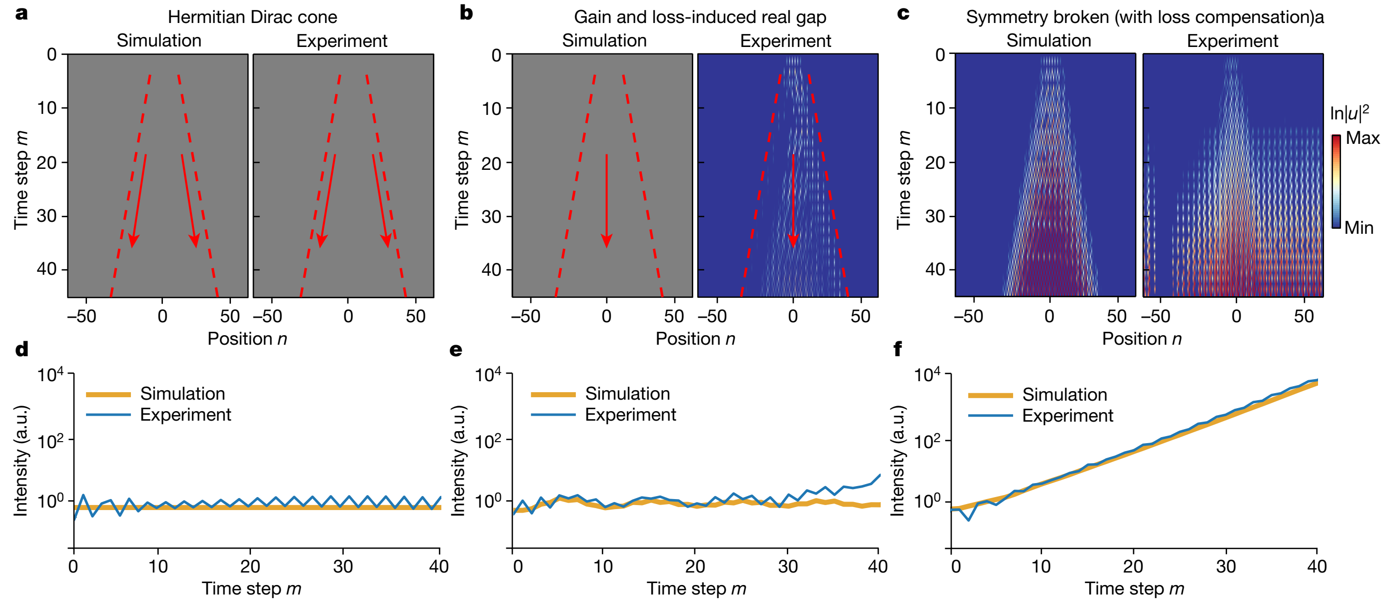

Fig. 2 | Evolution of a Gaussian wave packet in the synthetic lattice. **a**, Evolution in the Hermitian lattice ($g = 0$) for an initial wave packet centred at $k = 0, \phi = \pi$. Conical diffraction (red arrows) occurs in both simulations (left panel) and experimental data (right panel). **b**, Evolution in the non-Hermitian lattice ($g = 0.41$) corresponding to the massive relativistic quasiparticles of Fig. 1e. For the same initial wave packet as in **a**, the wavefunction spreads throughout the light cone (red arrows). Red dashes in **a** and **b** have slopes equal to the effective light speed $c = 1/\sqrt{2}$ (see Supplementary Information). **c**, Similar to **b** but with the initial wave packet centred at $k = \phi = \pi$, at which the band energies are non-real. **d**–**f**, Total intensity of the pulse train versus time step m. Conservation of total intensity in **e** shows that the non-Hermitian quasiparticles behave like Hermitian particles, unlike the exponential intensity increase seen in **f**. In **c** and **f**, we perform the experiment with a further loss on both fibre loops to avoid blow-up and compensate for the loss when plotting. a.u., arbitrary units.

$\theta = k = \pi, \phi = 0$, which we do not use). Here we plot only the quasienergy bands near the Dirac point; a full band diagram is shown in Extended Data Fig. 2.

Next, we apply gain and loss to the lattice. We first consider a trivial case as shown in the upper panel of Fig. 1d, in which the spatial period remains $\Delta n = 2$. The Dirac point turns into a pair of EPs (Fig. 1d, lower panel), joined by a 'bulk Fermi arc' along $\mathrm{Re}(\theta) = 0, \phi = \pi$ (ref. 35). Similar non-Hermitian band structures have been found in earlier works[36]. Near the bulk Fermi arc, $\mathrm{Im}(\theta) \neq 0$, so the quasiparticles blow up or decay over time.

Another gain and loss distribution with $\Delta n = 4$ is shown in the upper panel of Fig. 1e (the temporal period remains $\Delta m = 2$). The Floquet–Bloch ansatz still has the form in equation (4), but with a four-component wavefunction (see Supplementary Information). The spectrum now has a real quasienergy gap (Fig. 1e, lower panel). In the vicinity of $k = 0, \phi = \pi$, the two plotted bands are numerically verified to have exactly real θ. Moreover, they are governed by an effective Dirac Hamiltonian

$$H_{\mathrm{eff}} = M(g)\sigma_1 + \frac{1}{2}v_{\mathrm{D}}k\sigma_2 - v_{\mathrm{D}}(\phi - \pi)\sigma_3, \quad (5)$$

in which σ_1, σ_2 and σ_3 are the Pauli matrices, v_{D} is the Dirac velocity and $M(g) = \cosh(g - 1)$ is a real Dirac mass that varies with the gain and loss level (see Extended Data Fig. 3 and Supplementary Information). We also verified that the two participating bands are orthogonal (using the standard definition of the wavefunction inner product) for each k and ϕ. These properties result from an unbroken 'semi-Hermitian' symmetry, which protects both the real-valuedness of eigenvalues and the pairwise orthogonality of eigenvectors, as shown in previous theoretical works[22,23] (see Methods).

For Fig. 1e, note that the bands are not real everywhere: around $k = \pm\pi$, semi-Hermiticity is spontaneously broken[20] and the θs are complex.

Wave-packet evolution

To study how quasiparticles evolve in the synthetic lattice, we use a diffusion protocol to prepare pulse trains corresponding to Gaussian wave packets centred around some k, with ϕ and other parameters fixed (see Methods). We do not excite a specific band (which would involve specially preparing initial pulse sequences[37]); instead, the initial wave packet excites all Bloch states in all bands within a wavenumber window $\Delta k \approx 0.12\pi$.

For the Hermitian case ($g = 0$), with the initial wave packet centred at $k = 0$, the wavefunction spreads in two well-defined beams (Fig. 2a). Simulation results obtained through equation (2) (left panel) agree well with the experimental data (right panel). Such 'conical diffraction' is a signature of a massless relativistic quasiparticle[38]. The propagation speed is consistent with the effective light speed $c = 1/\sqrt{2}$ calculated from the Floquet band structure (see Supplementary Information). Note that the $g = 0$ case has two distinct bands, which form a Dirac cone. Figure 2d shows a logarithmic plot of the total intensity $I(m) = \sum_n (|u_n^m|^2 + |v_n^m|^2)$ versus m. The graphs for both simulation and experiment are approximately constant, consistent with energy conservation.

Next, we apply the semi-Hermitian gain and loss distribution of Fig. 1e, which is predicted to generate a real Dirac mass. For the same initial conditions, the conical diffraction disappears and the wavefunction instead spreads over the entire light cone (Fig. 2b). These results are consistent with theoretical expectations: in the two participating bands, the quasiparticles become massive and thus have a range of group velocities below the effective light speed. There are also two other bands, whose quasienergies are real near $k = 0$ (Extended Data Fig. 2c). In Fig. 2e, we see that the total intensity remains stable over long times, similar to the Hermitian case of Fig. 2d and consistent with the Bloch states having real quasienergies. The deviation between experimental and simulated intensities after $m > 30$ is attributable to imperfections in lattice parameter settings and noise accumulation[21,37].

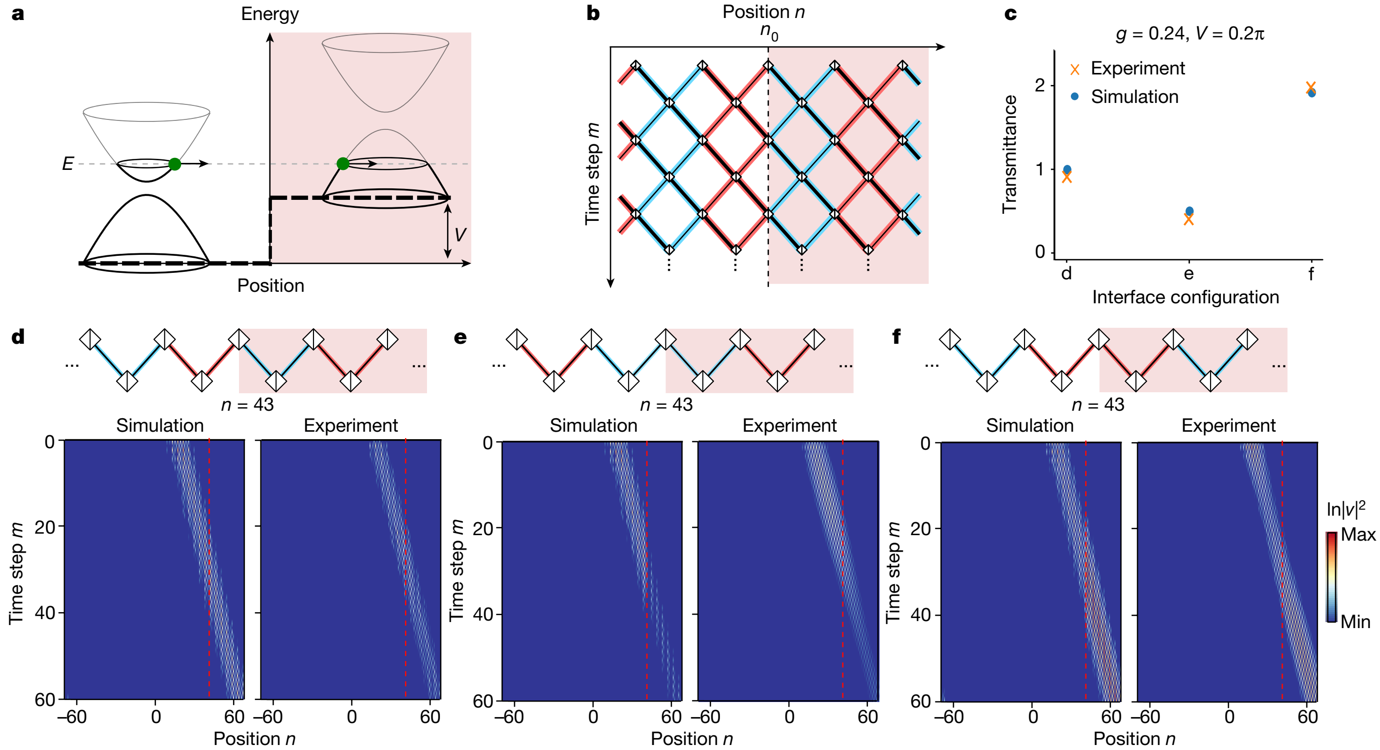

Fig. 3 | Klein tunnelling of massive Dirac quasiparticles. a, Schematic of Klein tunnelling with massive Dirac cones. An incident quasiparticle of energy E (left) impinges on a domain with scalar potential V (right). **b**, Schematic of a synthetic lattice with a gain and loss distribution supporting a massive Dirac cone. In the right domain, shaded in pink, a uniform scalar potential V is applied. **c**, Experimentally measured (crosses) and simulated (dots) transmittance for the lattice configurations shown in **d**–**f**. **d**–**f**, Scattering results. In all cases, the right domain has an extra scalar potential V, but the sites around the interface are laid out differently (top). In the simulated (bottom left) and experimentally measured (bottom right) intensity plots, reflection is found to be suppressed, whereas the transmittance is unity (**d**), damped (**e**) and amplified (**f**), respectively. The lattice parameters are $\phi = \pi$, $g = 0.24$ (which corresponds to $M \approx 0.03$), $k = 0.1\pi$ (which corresponds to $E \approx 0.02\pi$) and $V = 0.2\pi$.

For comparison, Fig. 2c shows the evolution for a wave packet centred at $k = \pi$, at which the bands have non-real quasienergies. All other parameters, including the initial conditions, are the same as in Fig. 2d. In the experiment, we apply a further uniform loss to both fibre loops to prevent an intensity blow-up and compensate for it when plotting (see Methods). The results reveal exponential amplification over time[39] (Fig. 2c,f).

Klein tunnelling of massive Dirac quasiparticles

Next, we investigate the Klein tunnelling of massive Dirac particles, as illustrated in Fig. 3a. In the Hermitian case, Dirac particles can efficiently cross potential barriers of height V exceeding Mc^2, with transmittance tending to unity as $V \to \infty$ (refs. 24,25). Semi-Hermitian Dirac quasiparticles, on the other hand, have been predicted to exhibit an anomalous form of Klein tunnelling in which energy conservation holds in the bulk but breaks down at the domain wall[23] (this is unrelated to the claim of greater-than-unity reflectance in Hermitian Klein tunnelling, which is an artefact of a redefinition of flux[25]). Here we demonstrate both kinds of effects. As shown schematically in Fig. 3b, we add an effective scalar potential barrier to the synthetic lattice (pink area) by means of a uniform phase modulation[40] (see Methods). There are several ways to configure the lattice boundary. In the baseline case (Fig. 3d), the wave packet incident from the left experiences nearly unity transmission, with reflection strongly suppressed. We also study alternative configurations in which the gain and loss is flipped across the boundary, keeping the sign of M unchanged. In such cases, the reflection is still strongly suppressed, but the transmitted beam is either amplified (Fig. 3e) or damped (Fig. 3f). This amplification or damping depends on the gain and loss of the boundary's central site and occurs only while the wave packet is impinging on the step. Within the bulk domains, the intensity is conserved because M is real. Our experimental results for the net transmittance are in excellent agreement with simulations, as shown in Fig. 3c.

Time reflection and refraction

The scattering of Dirac particles by time-dependent modulations is also of notable physical interest. In other metamaterial models, it has been shown that a wave experiencing an abrupt change in refractive index can undergo a splitting that is interpretable as time reflection and refraction[28–32,41]. Along similar lines, we consider the consequences of abruptly changing the mass, which is usually considered an intrinsic particle property. Specifically, we implement a temporal boundary that abruptly flips the sign of the Dirac mass M (Fig. 4a). Owing to translational invariance, k is conserved across the temporal boundary. For stationary Dirac particles ($k = 0$), the mass flip exactly interchanges the upper-band-edge and lower-band-edge eigenstates. In the non-relativistic limit, time reflection should thus occur as the quasiparticle is efficiently transferred to a negative-energy state with the opposite group velocity (see Supplementary Information). Intriguingly, this behaviour follows the simple intuition that, given a conserved non-relativistic momentum $p = Mv$, flipping the sign of M causes v to reverse. In the relativistic (large-k) limit, the mass flip should be negligible, allowing the particle to be transmitted strongly across the temporal boundary.

To implement this temporal boundary, we apply the lattice configuration shown in Fig. 4b. The gain and loss distributions are displaced by

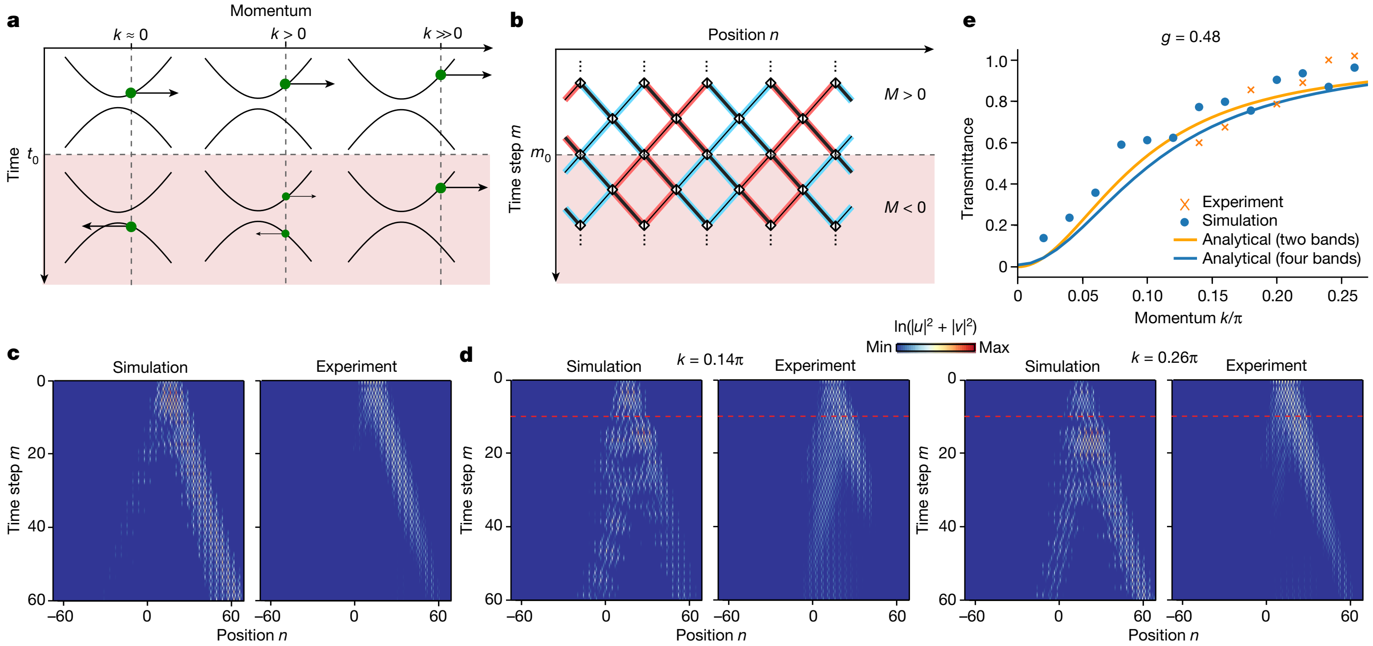

Fig. 4 | Time reflection and refraction of Dirac quasiparticles. a, Schematic of time reflection and refraction with massive Dirac cones. An incident quasiparticle of energy E (top) impinges on a temporal boundary that flips the sign of the Dirac mass (bottom). The value of the conserved momentum k determines the scattering behaviour. **b**, Lattice configuration implementing the mass-flipping temporal boundary. **c**, Simulated and experimental intensity plots showing the free propagation of the wave packet in the absence of the temporal boundary. **d**, Simulated and experimental intensity plots showing scattering from the mass-flipping temporal boundary (dashed red lines). Reflection is observed at small k and strong transmission at large k. **e**, Transmittance versus k based on experimental observations, lattice simulations, the non-Hermitian Dirac model (four bands) and the effective Hermitian Dirac model (two bands). The lattice parameters are $\phi = \pi$, $g = 0.48$ (which corresponds to $M \approx 0.12$) and $m_0 = 10$.

a quarter of a unit cell after $m_0 = 10$, reversing the sign of M (see Supplementary Information). In the absence of the temporal boundary, a Gaussian wave packet prepared with momentum k propagates with constant group velocity (Fig. 4c). With the temporal boundary, we observe strong reflection at small k (Fig. 4d, left) and strong transmission at large k (Fig. 4d, right), consistent with the arguments in the previous paragraph. Extracting the k-dependent transmission probabilities (using intensities at $m = 42$ (see Extended Data Fig. 9)), we find a good quantitative match with the predictions of the non-Hermitian continuum Hamiltonian (equation (5)), as well as the effective two-band Hermitian Dirac Hamiltonian, as shown in Fig. 4e.

Conclusion

In conclusion, we have demonstrated a non-Hermitian mechanism for generating real Dirac masses, using a synthetic photonic lattice containing optical gain and loss and Floquet modulations. Rather than being an intrinsic property, the Dirac mass can be engineered in space and time by varying the gain and loss, as we have demonstrated with our observations of non-Hermitian anomalous Klein tunnelling and the selective time reflection of massive Dirac quasiparticles. In the future, other exotic phenomena should be accessible with this experimental platform, such as non-Hermitian Landau levels[22] or relativistic momentum gaps[30]. Different varieties of relativistic quasiparticles may also be realizable using more complicated lattice designs[42].

Online content

Any methods, additional references, Nature Portfolio reporting summaries, source data, extended data, supplementary information, acknowledgements, peer review information; details of author contributions and competing interests; and statements of data and code availability are available at https://doi.org/10.1038/s41586-024-07664-x.

1. Wilczek, F. Origins of mass. *Cent. Eur. J. Phys.* **10**, 1021–1037 (2012).
2. Anderson, P. W. Plasmons, gauge invariance, and mass. *Phys. Rev.* **130**, 439–442 (1963).
3. Higgs, P. W. Broken symmetries and the masses of gauge bosons. *Phys. Rev. Lett.* **13**, 508–509 (1964).
4. Castro Neto, A. H., Guinea, F., Peres, N. M. R., Novoselov, K. S. & Geim, A. K. The electronic properties of graphene. *Rev. Mod. Phys.* **81**, 109–162 (2009).
5. Haldane, F. D. M. Model for a quantum Hall effect without Landau levels: condensed-matter realization of the "parity anomaly". *Phys. Rev. Lett.* **61**, 2015 (1988).
6. Kane, C. L. & Mele, E. J. Quantum spin Hall effect in graphene. *Phys. Rev. Lett.* **95**, 226801 (2005).
7. Hasan, M. Z. & Kane, C. L. *Colloquium*: Topological insulators. *Rev. Mod. Phys.* **82**, 3045–3067 (2010).
8. Qi, X.-L. & Zhang, S.-C. Topological insulators and superconductors. *Rev. Mod. Phys.* **83**, 1057–1110 (2011).
9. Aad, G. et al. Observation of a new particle in the search for the Standard Model Higgs boson with the ATLAS detector at the LHC. *Phys. Lett. B* **716**, 1–29 (2012).
10. Clay Mathematics Institute. Yang-Mills and the mass gap. *Clay Mathematics Institute* https://www.claymath.org/millennium/yang-mills-the-maths-gap/ (2023).
11. Bansil, A., Lin, H. & Das, T. *Colloquium*: Topological band theory. *Rev. Mod. Phys.* **88**, 021004 (2016).
12. Bergholtz, E. J., Budich, J. C. & Kunst, F. K. Exceptional topology of non-Hermitian systems. *Rev. Mod. Phys.* **93**, 015005 (2021).
13. Zaletel, M. P. et al. Colloquium: Quantum and classical discrete time crystals. *Rev. Mod. Phys.* **95**, 031001 (2023).
14. Bender, C. M. & Boettcher, S. Real spectra in non-Hermitian Hamiltonians having $\mathcal{PT}$ symmetry. *Phys. Rev. Lett.* **80**, 5243–5246 (1998).
15. Mostafazadeh, A. Pseudo-Hermiticity versus PT symmetry: the necessary condition for the reality of the spectrum of a non-Hermitian Hamiltonian. *J. Math. Phys.* **43**, 205–214 (2002).
16. Szameit, A., Rechtsman, M. C., Bahat-Treidel, O. & Segev, M. $\mathcal{PT}$-symmetry in honeycomb photonic lattices. *Phys. Rev. A* **84**, 021806 (2011).
17. Zhen, B. et al. Spawning rings of exceptional points out of Dirac cones. *Nature* **525**, 354–358 (2015).
18. Cerjan, A. et al. Experimental realization of a Weyl exceptional ring. *Nat. Photon.* **13**, 623–628 (2019).
19. Doppler, J. et al. Dynamically encircling an exceptional point for asymmetric mode switching. *Nature* **537**, 76–79 (2016).
20. Özdemir, Ş. K., Rotter, S., Nori, F. & Yang, L. Parity–time symmetry and exceptional points in photonics. *Nat. Mater.* **18**, 783–798 (2019).
21. Regensburger, A. et al. Parity–time synthetic photonic lattices. *Nature* **488**, 167–171 (2012).
22. Xue, H., Wang, Q., Zhang, B. & Chong, Y. D. Non-Hermitian Dirac cones. *Phys. Rev. Lett.* **124**, 236403 (2020).

23. Terh, Y. Y., Banerjee, R., Xue, H. & Chong, Y. D. Scattering dynamics and boundary states of a non-Hermitian Dirac equation. *Phys. Rev. B* **108**, 045419 (2023).
24. Holstein, B. R. Klein's paradox. *Am. J. Phys.* **66**, 507–512 (1998).
25. Dombey, N. & Calogeracos, A. Seventy years of the Klein paradox. *Phys. Rep.* **315**, 41–58 (1999).
26. Katsnelson, M. I., Novoselov, K. S. & Geim, A. K. Chiral tunnelling and the Klein paradox in graphene. *Nat. Phys.* **2**, 620–625 (2006).
27. Jiang, X. et al. Direct observation of Klein tunneling in phononic crystals. *Science* **370**, 1447–1450 (2020).
28. Bacot, V., Labousse, M., Eddi, A., Fink, M. & Fort, E. Time reversal and holography with spacetime transformations. *Nat. Phys.* **12**, 972–977 (2016).
29. Zhou, Y. et al. Broadband frequency translation through time refraction in an epsilon-near-zero material. *Nat. Commun.* **11**, 2180 (2020).
30. Lustig, E. et al. in *Proc. 2021 Conference on Lasers and Electro-Optics* (eds Kang, J. et al.) FF2H.1 (Optica Publishing Group, 2021).
31. Moussa, H. et al. Observation of temporal reflection and broadband frequency translation at photonic time interfaces. *Nat. Phys.* **19**, 863–868 (2023).
32. Dong, Z. et al. Quantum time reflection and refraction of ultracold atoms. *Nat. Photon.* **18**, 68–73 (2023).
33. Wimmer, M., Price, H. M., Carusotto, I. & Peschel, U. Experimental measurement of the Berry curvature from anomalous transport. *Nat. Phys.* **13**, 545–550 (2017).
34. Leykam, D., Rechtsman, M. & Chong, Y. Anomalous topological phases and unpaired Dirac cones in photonic Floquet topological insulators. *Phys. Rev. Lett.* **117**, 013902 (2016).
35. Özdemir, Ş. K. Fermi arcs connect topological degeneracies. *Science* **359**, 995–996 (2018).
36. Zeuner, J. M. et al. Observation of a topological transition in the bulk of a non-Hermitian system. *Phys. Rev. Lett.* **115**, 040402 (2015).
37. Wimmer, M. et al. Optical diametric drive acceleration through action–reaction symmetry breaking. *Nat. Phys.* **9**, 780–784 (2013).
38. Peleg, O. et al. Conical diffraction and gap solitons in honeycomb photonic lattices. *Phys. Rev. Lett.* **98**, 103901 (2007).
39. Miri, M.-A., Regensburger, A., Peschel, U. & Christodoulides, D. N. Optical mesh lattices with $\mathcal{PT}$ symmetry. *Phys. Rev. A* **86**, 023807 (2012).
40. Ye, H. et al. Reconfigurable refraction manipulation at synthetic temporal interfaces with scalar and vector gauge potentials. *Proc. Natl Acad. Sci. USA* **120**, e2300860120 (2023).
41. Lee, K. et al. Linear frequency conversion via sudden merging of meta-atoms in time-variant metasurfaces. *Nat. Photon.* **12**, 765–773 (2018).
42. Bukov, M., D'Alessio, L. & Polkovnikov, A. Universal high-frequency behavior of periodically driven systems: from dynamical stabilization to Floquet engineering. *Adv. Phys.* **64**, 139–226 (2015).

Methods

Experimental setup

A schematic of the experiment is shown in Extended Data Fig. 1. A distributed feedback laser diode operating at $\lambda = 1{,}550$ nm sends a continuous-wave signal into our system. To prevent backscattering into the laser source, an isolator is placed immediately after it. The input signal is shaped into rectangular pulses of width 100 ns by an electro-optical modulator. Subsequently, the signal is enhanced by an erbium-doped fibre amplifier (EDFA) and then cleaned up by a band-pass filter and a polarizer.

Before developing the signal into a synthetic lattice, we take further steps to stabilize the amplification provided by the EDFA, based on the protocol reported in ref. 21. A quasi-continuous train of pulses, each separated by roughly one round-trip time, is injected into both loops before the actual experiment. During this initial phase, the electro-optical modulators in both loops are set to 0% transmission, allowing the EDFAs to adapt to the input power level. After about 8 ms, we set the electro-optical modulator at the signal generation side to 0%, so that only the last pulse from the warm-up phase is retained for the experiment.

After the warm-up phase, the pulses begin to propagate within the coupled fibre loops. The average round-trip time is about 20 µs, with a difference of about 300 ns between the loops. To further stabilize the pulses, a strong pilot signal at 1,535 nm (the wavelength corresponding to the peak of EDFA emission spectrum) is applied in both loops immediately after the fibre spools. This signal can be cleaned by a following band-pass filter owing to its large wavelength difference with our operating wavelength of $\lambda = 1{,}550$ nm. Polarizers and polarizing beam splitters are used to ensure that only a single polarization is present in both loops.

We remotely control the electro-optical modulator and phase modulators to implement the gain and loss and phase-modulation profiles described in the main text. We also use these to implement absorbing boundary conditions for the synthetic lattice, by setting the transmission in both loops to 0% at the start or near the end of each round trip. These settings also help prevent noise build-up inside the loops.

To observe the wavefunction dynamics, we monitor the pulses circulating in each loop with photodiodes placed before the central coupler.

Semi-Hermitian Floquet band structures

The non-Hermitian Floquet band structures we consider (configuration in Fig. 1e) can host a massive Dirac Hamiltonian because of a pair of symmetries we call 'semi-Hermiticity'[22,23]. In terms of their action on a 4 × 4 evolution operator U, the symmetries are:

$$\Sigma_0 U \Sigma_0 = (U^{-1})^{\dagger} \tag{6}$$

$$\{\mathrm{i}U, \Sigma_3\Sigma_1 T\} = 0, \tag{7}$$

in which T is the complex conjugation operator and

$$\Sigma_\mu = \begin{bmatrix} 0 & \sigma_\mu \\ \sigma_\mu & 0 \end{bmatrix}, \quad \mu = 0, 1, 2, 3. \tag{8}$$

Here σ_0 is the 2 × 2 identity matrix, and σ_1, σ_2 and σ_3 are the Pauli matrices.

We first consider equation (6), which is an instance of pseudo-Hermiticity[15]. U has a set of right eigenvectors, obtained from the eigenproblem

$$U\,|\psi_n\rangle = \mathrm{e}^{-\mathrm{i}\theta_n}\,|\psi_n\rangle, \tag{9}$$

in which $\theta_n \in \mathbb{C}$ is the quasienergy. The corresponding left eigenvectors satisfy

$$\langle\phi_n|\;U = \langle\phi_n|\;\mathrm{e}^{-\mathrm{i}\theta_n} \tag{10}$$

$$\Rightarrow (U^{-1})^{\dagger}|\phi_n\rangle = \mathrm{e}^{-\mathrm{i}\theta_n^*}|\phi_n\rangle. \tag{11}$$

Therefore equation (6) implies that

$$U(\Sigma_0|\phi_n\rangle) = \Sigma_0(U^{-1})^{\dagger}|\phi_n\rangle = \mathrm{e}^{-\mathrm{i}\theta_n^*}(\Sigma_0|\phi_n\rangle). \tag{12}$$

Thus, for each solution to equation (9) with quasienergy θ_n, there is a solution with quasienergy θ_n^*. The quasienergies are either real or come in complex conjugate pairs.

Equation (7) is an instance of anti-$\mathcal{PT}$ symmetry. It is equivalent to

$$U^*\Sigma_3\Sigma_1 = \Sigma_3\Sigma_1 U. \tag{13}$$

Using this with equation (9) gives

$$\Sigma_3\Sigma_1 U|\psi_n\rangle = U^*\Sigma_3\Sigma_1|\psi_n\rangle = \mathrm{e}^{-\mathrm{i}\theta_n}\Sigma_3\Sigma_1|\psi_n\rangle \tag{14}$$

$$UT\Sigma_3\Sigma_1|\psi_n\rangle = \mathrm{e}^{\mathrm{i}\theta_n^*}T\Sigma_3\Sigma_1|\psi_n\rangle. \tag{15}$$

Hence, there is an eigenstate $T\Sigma_3\Sigma_1\;|\psi_n\rangle$ with quasienergy $-\theta_n^*$. Moreover, we can show that this is orthogonal to the original eigenstate, as follows: let

$$|\psi_n\rangle = \begin{pmatrix} p \\ q \end{pmatrix}, \tag{16}$$

in which p and q are two-component vectors. Then

$$\langle\psi_n|T\Sigma_3\Sigma_1|\psi_n\rangle = \begin{pmatrix} p^{\dagger} & q^{\dagger} \end{pmatrix}\begin{pmatrix} -\mathrm{i}\sigma_2 & 0 \\ 0 & -\mathrm{i}\sigma_2 \end{pmatrix}\begin{pmatrix} p^* \\ q^* \end{pmatrix} \tag{17}$$

$$= -\,\mathrm{i}(p^{\dagger}\sigma_2 p^* + q^{\dagger}\sigma_2 q^*) \tag{18}$$

$$= 0 \text{ for any } p, q. \tag{19}$$

Thus, the combination of equations (6) and (7) can produce behaviour analogous to Hermiticity. If the pseudo-Hermiticity equation (6) is unbroken, then equation (7) implies the existence of pairs of orthogonal eigenstates with real eigenvalues $(\theta_n, -\theta_n)$, in which $\theta_n \in \mathbb{R}$ (ref. 22).

We thus see that the combination of two non-Hermitian symmetry conditions—unbroken pseudo-Hermiticity and anti-$\mathcal{PT}$ symmetry—yield the two features (real eigenvalues and pairwise orthogonal eigenvectors) consistent with the existence of an effective Dirac Hamiltonian. Satisfying both conditions simultaneously requires at least a 4 × 4 matrix; hence, apart from the two orthogonal bands participating in the Dirac cone, there are two other auxiliary bands (which are, likewise, orthogonal to each other).

Note that a 2 × 2 matrix cannot give this behaviour. In the 2 × 2 case, having two real eigenvalues with orthogonal eigenvectors implies that the Hamiltonian is Hermitian (for a 2D vector space, pairwise orthogonality simply implies that the two eigenvectors form an orthogonal basis).

State preparation

For the experiments in Fig. 2, we prepare initial wave packets designed to excite quasiparticles around a target momentum k. This is achieved using the procedure described in ref. 37. We start with a single pulse produced by the previously described signal-generation system. This is allowed us to evolve according to the evolution equations

$$u_n^{m+1}=\frac{1}{\sqrt{2}}\,(u_{n+1}^{m}+\mathrm{i}v_{n+1}^{m})\,\mathrm{e}^{\mathrm{i}\phi_0}F(m) \tag{20}$$

$$v_n^{m+1}=\frac{1}{\sqrt{2}}\,(\mathrm{i}u_{n-1}^{m}+v_{n-1}^{m})\,, \tag{21}$$

in which

$$F(m)=m(\mathrm{mod}2). \tag{22}$$

This is equivalent to fully absorbing the signal inside the short loop in every two time steps. To select the Bloch modes at wavenumber k, we choose the phase modulation ϕ_0 such that

$$k=2\pi+2\phi_0. \tag{23}$$

Extended Data Fig. 4a shows the evolution of the pulses and Extended Data Fig. 4b shows the intensity distribution at the end of the preparation stage ($m=55$). The experimental results are clearly in excellent agreement with simulations, as well as fitting a Gaussian envelope

$$f(n)=A\exp\left[-\frac{(n-n_0)^2}{2\sigma^2}\right], \tag{24}$$

in which n_0 is the centre of the wave packet and σ is its spatial width. In our case, $\sigma\approx3.7$, corresponding to a spectral width of $\delta\theta\approx0.12\pi$.

Investigating states with complex quasienergies

In Fig. 2c,f, we plot the time evolution of a wave packet centred at $k=\pi$, at which the band quasienergies are non-real. In contrast to the $k=0$ case, in which the quasiparticles behave like energy-conserving Dirac particles, in this case, the wavefunction is predicted to undergo exponential amplification.

Experimentally, it is not desirable to access the amplifying regime, as the amplification of the EDFAs will saturate[21]. To bypass this problem, we use a simple compensation method previously used, for example, in ref. 43. We apply an extra loss, which is uniform in both space and time, to both loops, at a loss level that maintains nearly constant overall power throughout the experiment (based on the photodetector observations). The evolution equations are modified to

$$u_n^{m+1}=\frac{1}{\sqrt{2}}(u_{n+1}^{m}+\mathrm{i}v_{n+1}^{m})\mathrm{e}^{\mathrm{i}\Phi(m)}F(n)\mathrm{e}^{-\gamma/2} \tag{25}$$

$$v_n^{m+1}=\frac{1}{\sqrt{2}}(\mathrm{i}u_{n-1}^{m}+v_{n-1}^{m})F(n-1)\mathrm{e}^{-\gamma/2}, \tag{26}$$

in which $\exp(-\gamma/2)$ is the damping factor over one time step. The uniform loss does not alter the band structure, apart from adding a constant imaginary part to the quasienergy of every eigenstate, equivalent to a spatially uniform decay factor $\exp(-\gamma/2)$.

In Extended Data Fig. 5, we plot the Fourier spectra obtained from the numerically simulated evolving wavefunctions for the three different unit-cell configurations of Fig. 1c–e with $\phi=\pi$. The results show good agreement with the theoretical Floquet band structures (the imaginary parts of the bands manifest as bright regions in the Fourier spectra). Experimentally accessing the corresponding phase information is impractical with our current system parameters; with a 20 μs average round-trip time and 8 ms warm-up interval, a reference field with coherence length of up to 200 km would be required.

In Extended Data Fig. 6a, we plot the raw (uncompensated) time evolution of a wave packet subject to this uniform loss. The total intensity does not undergo exponential amplification, as shown in Extended Data Fig. 6b. We then multiply the wavefunctions by $\exp(\gamma m/2)$ to produce the experimental data shown in Fig. 2.

Topological nature of the Dirac mass

One of the most remarkable features of massive Dirac quasiparticles is that they act as 'building blocks' for topological band insulators. A massive 2D Dirac Hamiltonian, equation (5), contributes $\pm\mathrm{sgn}(m/2)$ to the Chern numbers of the two participating bands[5]. When there are two adjacent domains with opposite signs of m, topological states appear at the boundary[44,45].

To show that the gain and loss-induced Dirac masses can similarly create topological boundary states, we implement a lattice consisting of two domains whose gain and loss distributions are displaced relative to each other by a quarter of a unit cell (Extended Data Fig. 7a). From the derivation of the Floquet band structure, we can show that this displacement flips the sign of M (see Supplementary Information). (In an earlier theoretical analysis of a non-Hermitian 1D topological lattice, a similar displacement was also shown to induce a topological transition[46]). In Extended Data Fig. 7b, the quasienergy bands for a finite sample are plotted against ϕ (which serves as a momentum-like variable). This reveals a branch of boundary states spanning the gain and loss-induced bandgap. They have a chiral dispersion relation, as expected of the topological boundary states generated by a Dirac mass inversion, even though $\mathrm{Im}(\theta)$ does not strictly vanish because the domain wall breaks the semi-Hermitian symmetry[46]. From the spatial distributions (Extended Data Fig. 7c), we see that the localization length is affected by the gain and loss level g, which governs the size of the bulk gap. We emphasize that these topological boundary states are only induced by gain and loss, because the bulk gap is closed for $g=0$.

To examine this phenomenon experimentally, we inject a single initial pulse at the boundary ($n=0$), which has strong spatial overlap with the boundary states. In Extended Data Fig. 7d, we plot the intensity distribution for $g=0.41$ (blue circles), obtained by a normalized time average of $|u_n^m|^2+|v_n^m|^2$. The profile fits the theoretically calculated spatial distribution for the boundary state (red line). Finally, from the time-evolution data for different values of g (Extended Data Fig. 7e–g), we observe that the localization length decreases with g, in agreement with Extended Data Fig. 7c.

Klein tunnelling setup

Here we provide further details about the Klein tunnelling results shown in Fig. 3. In these experiments, we use an initial wave packet at $k=0.1\pi$ with a preparation stage of time step $m=105$. To form the barrier, we follow the method in ref. 40: instead of having a single phase modulator in the short loop, another phase modulator is added to the long loop. The evolution equation is then modified to

$$\begin{aligned}u_n^{m+1}&=\frac{1}{\sqrt{2}}(u_{n+1}^{m}+\mathrm{i}v_{n+1}^{m})F(n)\mathrm{e}^{\mathrm{i}\Phi(m)-\mathrm{i}V/2},\\ v_n^{m+1}&=\frac{1}{\sqrt{2}}(\mathrm{i}u_{n-1}^{m}+v_{n-1}^{m})F(n-1)\mathrm{e}^{-\mathrm{i}V/2},\end{aligned} \tag{27}$$

in which V denotes the scalar potential (in Fig. 3, we use $V=0.2\pi$). The factor of 1/2 is because of the Floquet unit cell having a time step of 2. The transmittance and intensity plots for other values of V are shown in Extended Data Fig. 8.

In Fig. 3c and Extended Data Fig. 8b, we plot the transmittance and reflectance, which, respectively, correspond to the intensities summed over sites to the right and left of the interface. These intensities are evaluated at time step $m=60$, after the scattering process has completed. One complication is that, during the wave-packet-preparation stage, as well as the right-propagating wave packet (residing in the upper band), we also excite pulses of the opposite propagation direction (residing in the lower band), as shown in the short-loop intensity evolution in Extended Data Fig. 8c–e. These extra excitations do not participate in the scattering process and are excluded when finding the reflectance and transmittance.

Data availability

The experimental data are available in the data repository for Nanyang Technological University at https://doi.org/10.21979/N9/0KBPTS. Other data supporting the findings of this study are available from the corresponding authors on reasonable request.

43. Weidemann, S., Kremer, M., Longhi, S. & Szameit, A. Topological triple phase transition in non-Hermitian Floquet quasicrystals. *Nature* **601**, 354–359 (2022).
44. Jackiw, R. & Rebbi, C. Solitons with fermion number ½. *Phys. Rev. D* **13**, 3398–3409 (1976).
45. Angelakis, D. G., Das, P. & Noh, C. Probing the topological properties of the Jackiw-Rebbi model with light. *Sci. Rep.* **4**, 6110 (2014).
46. Takata, K. & Notomi, M. Photonic topological insulating phase induced solely by gain and loss. *Phys. Rev. Lett.* **121**, 213902 (2018).

Acknowledgements This work was supported by the Singapore Ministry of Education (MOE) Tier 1 Grant No. RG148/20, Singapore Ministry of Education Academic Research Fund Tier 2 Grant No. MOE-T2EP50123-0007 and by the National Research Foundation (NRF), Singapore under Competitive Research Programme NRF-CRP23-2019-0007 and NRF-CRP23-2019-0005, and NRF Investigatorship NRF-NRFI08-2022-0001. C.S. and R.G. acknowledge the support of the Quantum Engineering Programme of the Singapore National Research Foundation, grant number NRF2021-QEP2-01-P01. H.X. acknowledges the support of the start-up fund and the direct grant (Grant No. 4053675) from The Chinese University of Hong Kong.

Author contributions H.X., B.Z. and Y.D.C. conceived the idea. H.X., L.Y., R.G. and E.A.C. designed and performed the experiment. L.Y. and R.G. analysed the data. C.S., B.Z. and Y.D.C. supervised the project. H.X., L.Y., R.G., Y.Y.T., C.S., B.Z. and Y.D.C. contributed to the discussion of the results and writing of the manuscript.

Competing interests The authors declare no competing interests.

Additional information

Supplementary information The online version contains supplementary material available at https://doi.org/10.1038/s41586-024-07664-x.

Correspondence and requests for materials should be addressed to Cesare Soci, Baile Zhang or Y. D. Chong.

Peer review information *Nature* thanks the anonymous reviewers for their contribution to the peer review of this work.

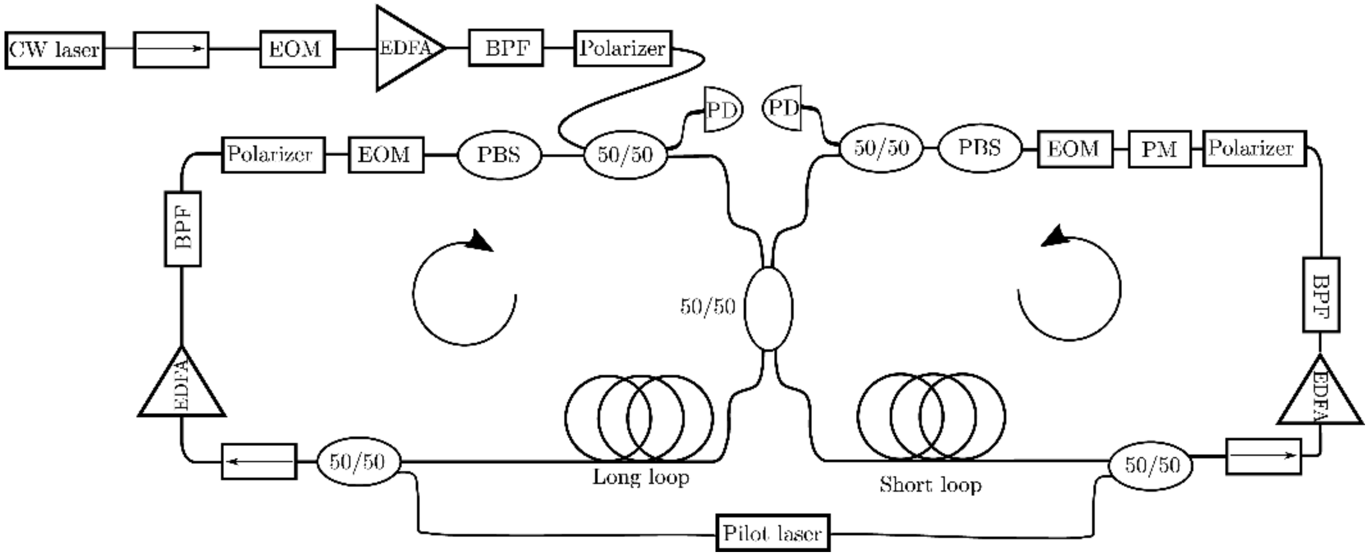

Extended Data Fig. 1 | Schematic of the experiment. The abbreviations are as follows: BPF, band-pass filter; CW, continuous wave; EDFA, erbium-doped fibre amplifier; EOM, electro-optical modulator; PBS, polarization beam splitter; PD, photodetector; PM, phase modulator. The boxes containing arrows denote isolators and the ovals labelled '50/50' and '90/10' denote optical couplers with the indicated splitting ratios.

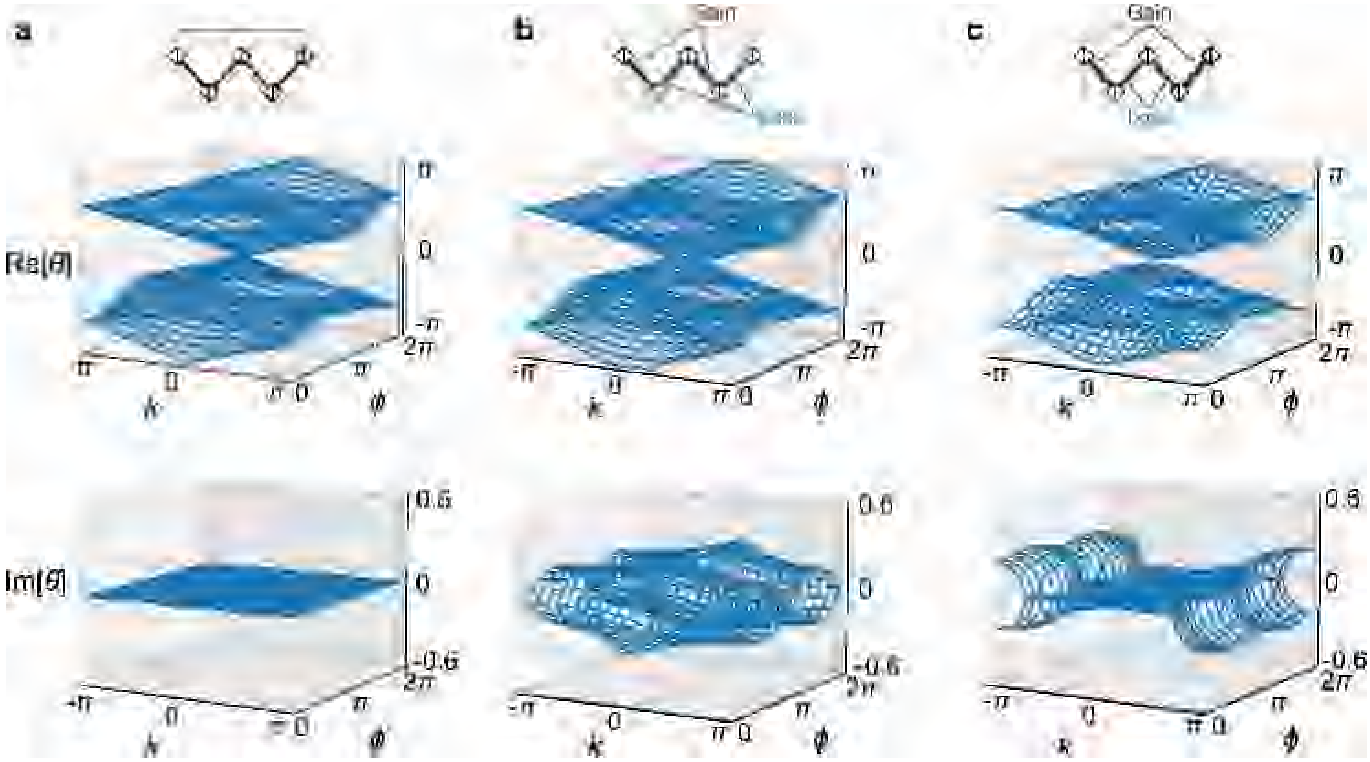

Extended Data Fig. 2 | Floquet band diagrams of the synthetic lattice for different gain/loss and phase distributions. **a**, No gain/loss ($g = 0$). **b**, Gain/loss/gain/loss. The Dirac point turns into a pair of EPs. The band energies are non-real at $k = 0$, $\phi = \pi$, whereas the band energies close to $k = \pm\pi$, $\phi = \pi$ are real. **c**, Gain/loss/loss/gain. At $k = 0$, $\phi = \pi$, there are two orthogonal bands with real band energies, governed by a massive Dirac Hamiltonian. In **b** and **c**, the gain/loss level is $g = 0.41$.

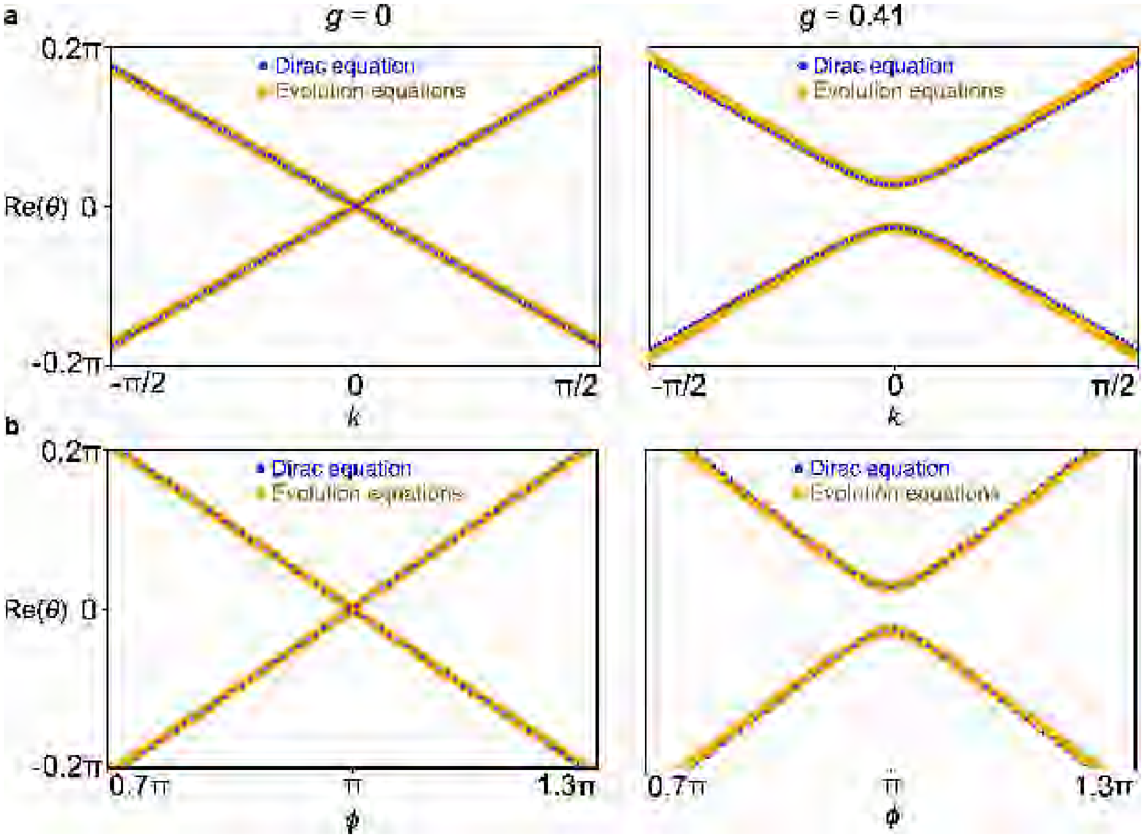

Extended Data Fig. 3 | Dispersion relation for the Dirac quasiparticles. These Floquet band diagrams are calculated using the evolution equations (orange) and the effective Dirac Hamiltonian (blue; see Supplementary Information), for $g = 0$ (left) and $g = 0.41$ (right). **a**, Quasienergies versus k. **b**, Quasienergies versus ϕ.

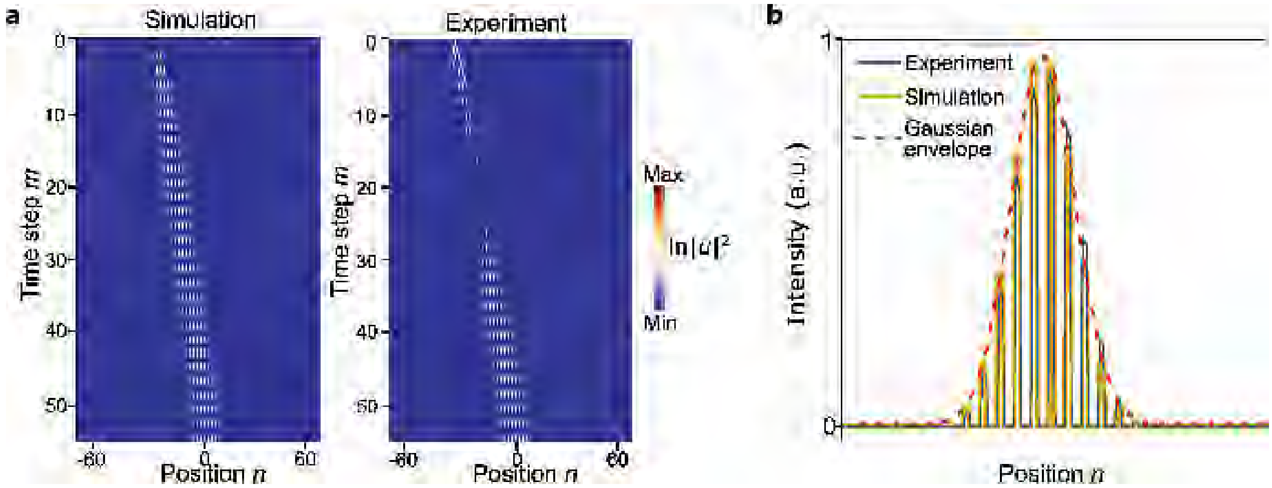

Extended Data Fig. 4 | Preparation of pulse train for exciting quasiparticles. a, Time evolution of a single initial pulse under equations (20)–(23), for $\phi_0 = -\pi$. **b**, Intensity profile at $m = 55$.

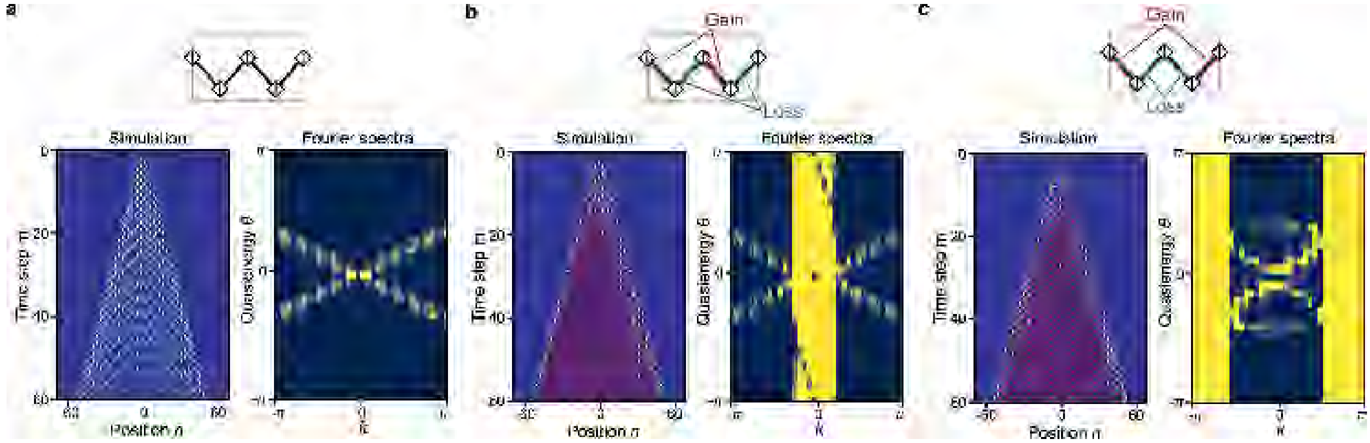

Extended Data Fig. 5 | Optical energy evolution and Fourier spectra for different gain/loss and phase distributions. **a**, No gain/loss ($g = 0$), $\phi = \pi$. **b**, Gain/loss/gain/loss, $\phi = \pi$, $g = 0.4$. **c**, Gain/loss/loss/gain at $k = 0$, $\phi = \pi$, $g = 0.4$. In **a**–**c**, the simulated intensity evolutions are obtained with a single pulse injection in the long loop at time $m = 0$. In each subplot, the Fourier spectra are derived from Fourier transformation of the simulation results on the left. All the other parameters are the same as these in experiments.

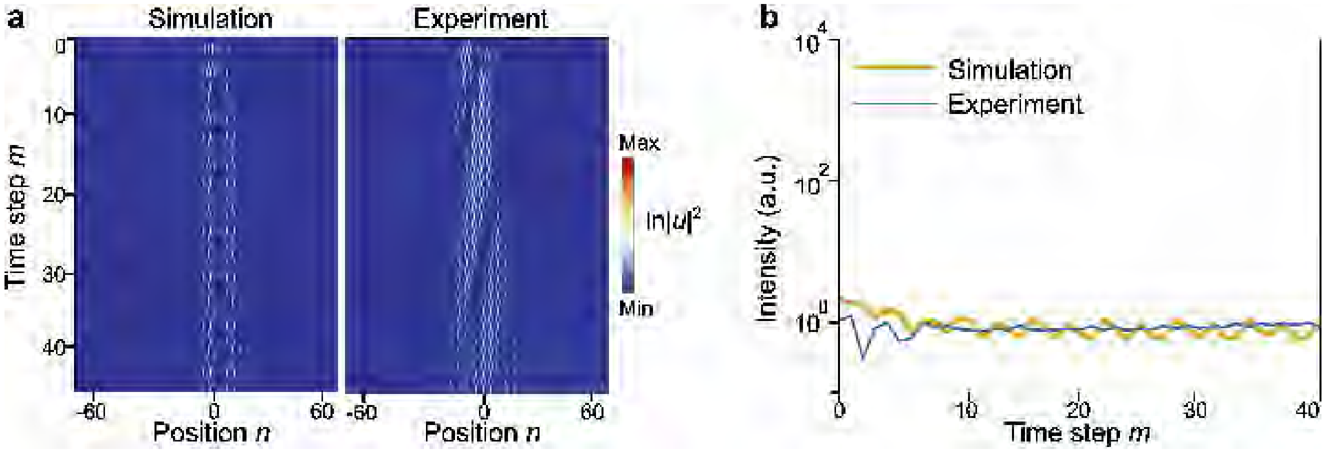

Extended Data Fig. 6 | Pulse propagation in the symmetry-broken regime. **a**, Raw data showing the evolution of a wave packet centred at $k = \pi$, with $g = 0.4055$, $\phi = \pi$ and uniform loss rate $\gamma = 0.223$. **b**, Plot of the total intensity in the short loop versus m.

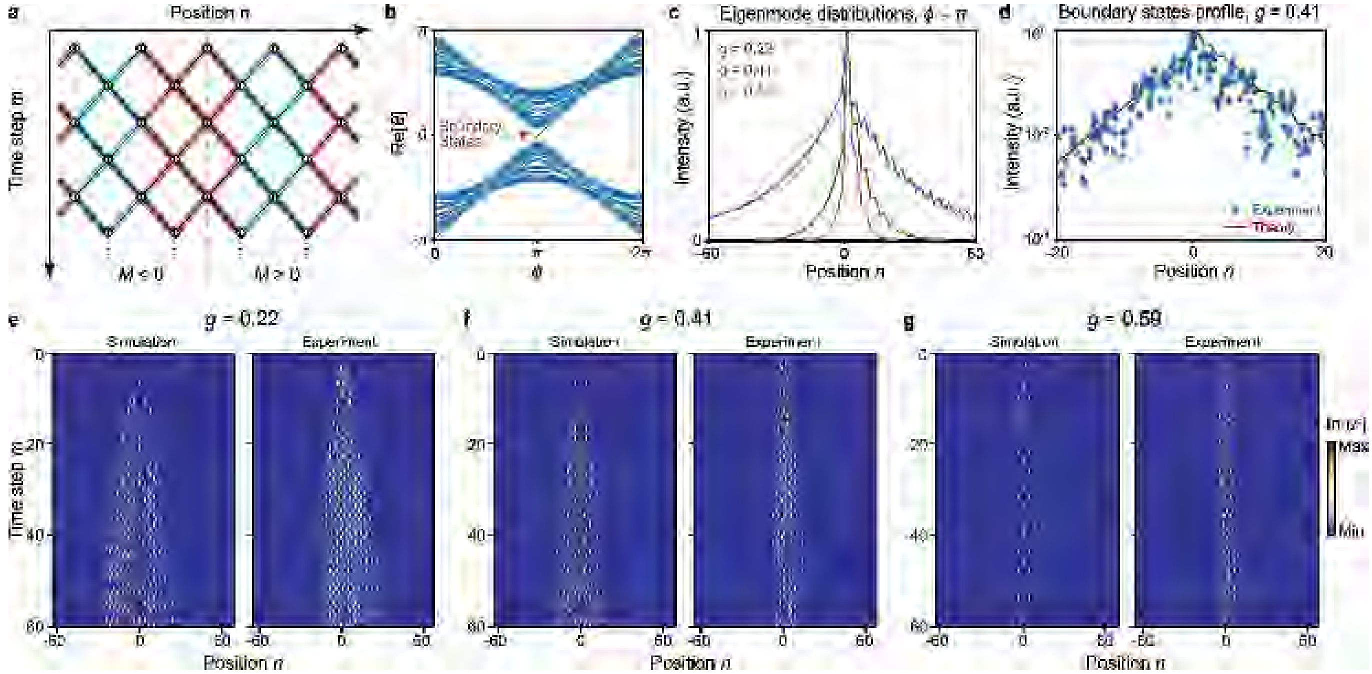

Extended Data Fig. 7 | Boundary states induced by gain and loss. **a**, Schematic of a synthetic lattice with two domains separated by a boundary (dashes). The effective Dirac Hamiltonians have mass $M < 0$ and $M > 0$ in the left and right domains, respectively. Here the colour represents the pseudospin of the Dirac quasiparticle, which is derived from the inner product between the eigenvector and the eigenvector of a massless Dirac Hamiltonian (the branch with positive group velocity). **b**, Floquet band diagram for a finite sample of the lattice shown in **a**, with total size $N = 59$ and gain/loss level $g = 0.59$. A chiral dispersion relation, corresponding to gain/loss-induced boundary states, spans the gap. **c**, Spatial distribution of $|u_n|^2 + |v_n|^2$ for the mid-gap boundary state, calculated with different values of g. **d**, Spatial profiles of $|u_n^m|^2 + |v_n^m|^2$ for the theoretical boundary eigenstate for $g = 0.41$ (red line) and the corresponding experimental data time-averaged over $40 \le m \le 70$ (blue dots). In **c** and **d**, we normalize the maximum intensity for individual subplots to 1. **e**–**g**, Time evolution of a pulse injected at $n = 0$, for $g = 0.22$, 0.41 and 0.59. In simulations (left panels) and experimental data (right panels), the pulse spreads into a wavefunction localized at the boundary, with localization length following the trend shown in **c**. In **c**–**g**, we set $\phi = \pi$.

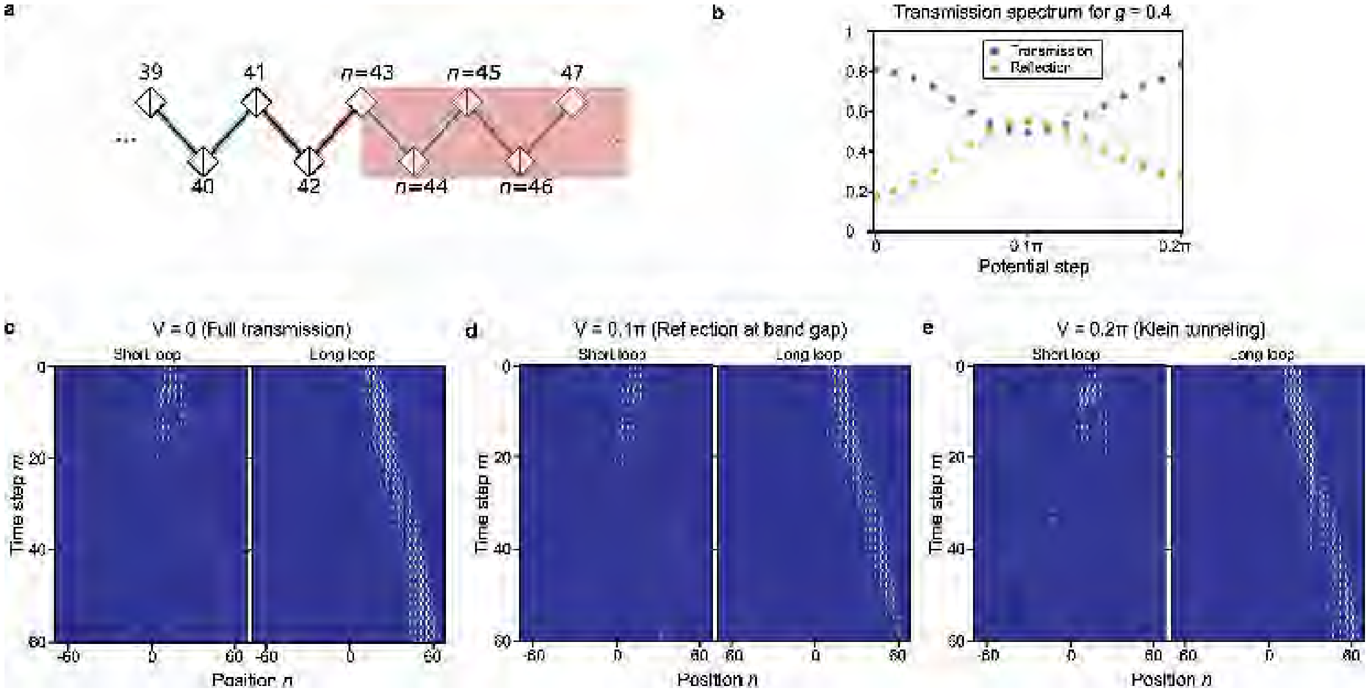

Extended Data Fig. 8 | Pulse propagation at different potential barrier heights. **a**, Schematic of the lattice configuration near the interface. **b**, Transmission and reflection coefficient as a function of potential *V*. **c**–**e**, Simulated intensity evolution as the potential barrier varies from 0 to 0.2π. In **c**–**e**, we set $\phi = \pi$, $g = 0.4$ (which corresponds to $M \approx 0.08$) and $k = 0.1\pi$ (which corresponds to $E \approx 0.03\pi$).

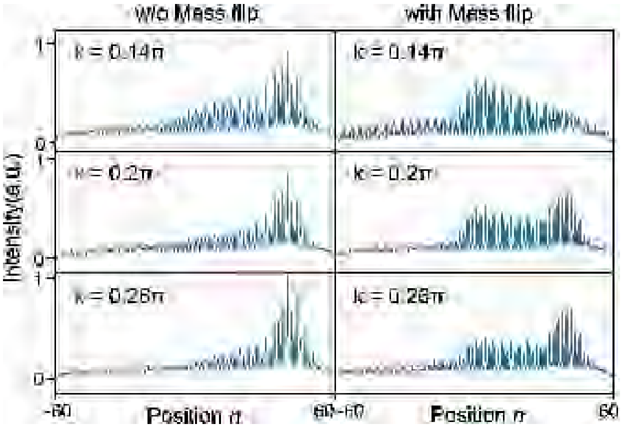

Extended Data Fig. 9 | Pulse profile at time step *m* = 42. Total intensity distribution with Gaussian pulse excitations of different momentum *k*. A temporal boundary is introduced at *m* = 10 for the right subplot. For all figures, we set $\phi = \pi$ and $g = 0.48$.